Title: Bending collapse analysis for thin and medium-thin-walled square and rectangular hollow shapes

Authors: Daniel Lavayen Farfan - María Jesús López Boada - Jorge A. Rodríguez Hernández

Version of record available online at
https://doi.org/10.1016/j.tws.2021.107934

Bending collapse analysis for thin and medium-thin-walled square and rectangular hollow shapes

Daniel Lavayen Farfan[a,b,*], Maria Jesus L. Boada[a], Jorge A. Rodriguez Hernandez[b]

[a] *Department of Mechanical Engineering - Research Institute for Vehicle Safety (ISVA), Carlos III University of Madrid. de la Universidad Ave., 30, 28911 Leganes, Madrid, Spain*
[b] *Section of Mechanical Engineering, Pontifical Catholic University of Peru. Universitaria Ave., 1801, 15088 San Miguel, Lima, Peru*

Abstract

Thin-walled hollow shapes are of great interest in many industries with weight constraints due to their availability, low price, and strength to weight ratio. However, they are also prone to localized bending collapse, which can be used as an energy absorption mechanism during deformation. Up until now, industrial applications have relied on numerical simulations, non-standardized tests, and a handful of theories to address the bending collapse behavior. In this paper, a modification to the most widely used theory is presented and adapted for hollow shapes with greater thickness that cannot be considered "thick. To verify the accuracy of the proposed modifications, a comparison with a detailed FEM model, validated through various three-point bending collapse experimental tests, has been performed. The results seem to show that the proposed modifications can predict the maximum load and collapse stage behavior of hollow shapes with more accuracy than the original analytical model. Thus, the proposed modification may be used to predict the collapse behavior of commercially available square and rectangular hollow shapes in different fields of application.

Keywords: bending collapse, three-point bending test, thin-walled collapse,

*Corresponding author
Email address: dlavayen @ pucp.edu.pe (Daniel Lavayen Farfan)

collapse analytical model, three-point bending collapse, medium-thin-walled shapes

1. Introduction

One of the design rules of lightweight design consists of using the full load capacity of the material [1, 2]. This means that unlike classical mechanical design where only the elastic region is taken into consideration for calculations, lightweight design also considers the plastic deformation regions of the material to take the material to its maximum load capacity. This is particularly useful in the automotive and aerospace industries, where structures have to be light and, at the same time, able to withstand high loads and to absorb the kinetic energy from impacts and collisions. The absorption of energy is typically performed by plastic deformations. For instance, the superstructure of a bus or coach must be able to absorb the kinetic energy from an impact and dissipate it as plastic deformations in certain parts of the structure. However, if this deformation is too large, then the deformed structure may crush the passengers, resulting in severe injury or death. Therefore, a correct and accurate calculation of the plastic and even collapse behavior of the structures and materials is needed, especially in the early stages of design.

When working with light structures, thin-walled, hollow shapes are preferred since they provide acceptable resistance and stiffness with low weight. Steel square hollow shapes (SHS) and rectangular hollow shapes (RHS) are extensively used in numerous manufacturing industries with weight constrains and high load requirements because of their availability, relatively low price, and different sizes. The problem with these structural shapes is that, due to their thin walls, they are prone to localized plastic collapse when a large bending moment is applied. It has been found, however, that localized collapse is a major energy absorption mechanism in these structures. The main difficulty with studying this failure mechanism is that “classical” theories cannot describe it,

since it happens at a specific zone of the structure. Numerical simulations and experimental tests are an option and have been proven to offer accurate results, but they are often time-intensive and/or expensive, thus inadequate in the early stages of design. There has also been a handful of theoretical analyses devoted to bending collapse.

The earliest works by Kecman [3, 4], in the 1980s, have set the basis of study of bending collapse and were performed in order to assess the energy absorption of thin-walled RHS used in structures for buses. Also during those years, Wierzbicki and Abramowicz [5, 6, 7] performed a more detailed study on axial and bending collapse of hollow shapes and found certain similarities between both. Later works by Kim and Reid [8], Shin et al. [9], Liu et al. [10], Kim et al. [11] as well more recent ones by Huang et al. [12, 13], offered different analytical approaches to the bending collapse of thin-walled shapes, all based on Kecman's work, addressing its limitations, offering corrections, and even expanding to include composite reinforcements. The bending collapse phenomenon has been validated through extensive experimentation and numerical simulations. However, even after addressing its limitations, Kecman's original model is still used by many researchers and engineers to study the bending collapse of thin-walled closed shapes. The main way to address the collapse behavior is through a bending moment - angle ($M - \theta$) curve for the plastic hinge that forms in the component under bending load, as well as the maximum moment reached and area under the curve, which consists of the energy absorbed through plastic deformation.

Experimental setups to determine the collapse behavior through the $M - \theta$ curves have also changed during the years. The earliest test rigs consisted of a cantilever beam setup. In this configuration, the free end of the cantilever is loaded through a system of cables and pulleys. The fixed end is either clamped to larger I-shapes fixed to the ground or casted into a concrete block. These testing rigs have been used by Kecman [3] and Brown and Tidbury [14]. However,

later research works have moved to a simpler setup consisting of a three-point bending test of the corresponding hollow shape. Authors such as Lee et al. [15, 16], Liu and Day [10], Ruiz et al.[17], Eksi and Genel [18], Kadir et al. [19], Phadatare and Hujare [20], Liu et al. [21], Huang et al. [12, 22, 23, 13], Xie [24], among others have used the three-point bending test. The advantage of using a three-point bending setup is that it can be easily installed on almost any universal testing machine; unlike the cantilever test setup, which requires additional preparations for the fixed support and load application. Moreover, Kecman's theory, despite having been tested and corroborated with a cantilever test, has also been used to compare results with three-point bending test results.

Currently, the only instance, with cantilever-like setups, is to assess the energy absorption in structural nodes of buses, according to the UN/ECE Regulation 66 [25] for the rollover test of bus structures. Although this method is more frequently used in the industry and testing institutions, there has been research based on these test setups, such as Hashemi et al. [26], Liang et al. [27, 28, 29], Rincon et al. [30], all related to bus structures. Both test methods (cantilever bending and three-point bending) generally seem to produce similar results under certain circumstances.

It is also worth noting that a formal definition of how thin are thin-walled shapes has yet to be found. The most important factor is not the thickness itself but thickness-to-height ratio (t/b). Most of the aforementioned authors, who focus on collapse theories for thin-walled hollow shapes, typically analyze hollow shapes with a thickness-to-height ratio lower than 0.03. However, not much research has been found that focuses on ratios $0.03 < t/b < 0.1$, which are typically commercially available and can still be considered thin and used by numerous manufacturers.

2. Theoretical analysis

2.1. Basic collapse theory

As mentioned before, the bending collapse theory developed by Kecman [3] is still widely used to obtain the theoretical $M-\theta$ curve for thin-walled SHS and RHS under bending, in general to develop lightweight structures. The original model, shown in Fig. 1, considers that the plastic deformations during collapse are concentrated along the numerous hinge lines and requires information from experimental tests, namely, the rolling radius along the hinge lines and the so-called nominal flow stress. Due to the repeatability of the collapse phenomenon in hollow steel structures, an empirical expression for the rolling radius has been suggested [3]. Moreover, the nominal flow stress was initially approximated to the ultimate strength of the material by Kecman [3]. Since the plastic deformation occurs mainly along the hinge lines, the energy absorbed by such lines W_i can be calculated as a function of the angle θ and used to determine the $M-\theta$ curve through numerical derivation as follows:

$$M(\theta) := \frac{d}{d\theta} W_{total}(\theta) \approx \frac{W_{total}(\theta + \Delta\theta) - W_{total}(\theta)}{\Delta\theta} \tag{1}$$

where $W_{total} = \sum_{i=1}^{8} W_i$ (each term W_i is described in Eq. 19 to 26 in the Appendix).

Each of the work terms W_i can be described depending on the hinge bending moment. In order to assess it, the hinge bending moment per unit length m_p, which depends on the flow stress σ_0, is defined.

$$m_p = \frac{1}{4}\sigma_0 t^2 \tag{2}$$

The original theory by Kecman [3] has been proven to give a fairly good approximation for the collapse response of SHS and RHS. However, three major limitations have been encountered when applying it to medium-thin-walled shapes, defined by the authors as those with thickness-to-height ratios in the range of $0.03 < t/b < 0.1$, which are used by many manufacturers and cannot

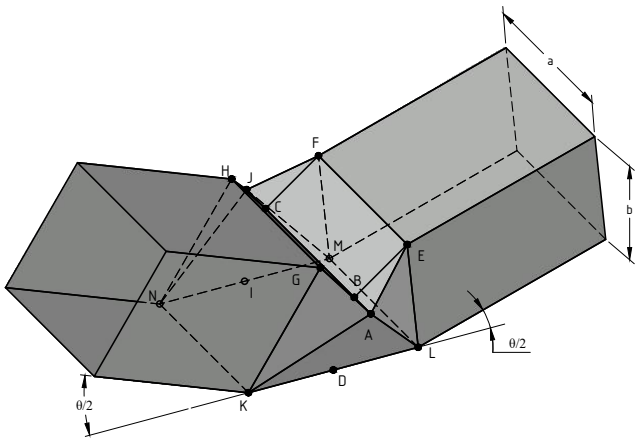

Figure 1: Original theoretical model by Kecman [4].

be defined as thick-walled. The first encountered limitation seemingly comes from the fact that Kecman's theory considers that all points in the through-the-thickness direction go into yielding at the same time, which is not the case for the medium-thin-walled shapes. Most of the surveyed literature focuses on ratios of t/b in the range of $t/b < 0.03$, where this assumption is fairly acceptable. Furthermore, the second limitation is related to the material model used. Most of the surveyed research has been performed with materials that can be represented fairly well with a elastic-perfectly plastic behavior. Even when this is not an explicit assumption of Kecman's model, the fact that certain terms of the energy absorbed by the hinge lines are expressed in terms of a constant flow stress, regardless of the deformation, shows that it is in fact an "implicit" assumption. Since material models with plastic hardening are not fully contemplated, some modification in the original model is required. This is especially important, since the maximum moment may be significantly underestimated for thicker shapes. Finally, the third and last limitation encountered is related to the fact that Kecman's model only considers the $M - \theta$ after the maximum moment is reached, in other words, it only considers the collapse stage. The energy absorbed before reaching this point is assumed to be negligible as it corresponds to elastic deformations with a minuscule rotation angle θ_m, where

the maximum moment M_m occurs. In other words, θ_m is set to zero and only plastic angles are plotted. This approximation may be adequate for thin-walled shapes, however, it no longer applies when the thickness increases, as shown in Fig. 2.

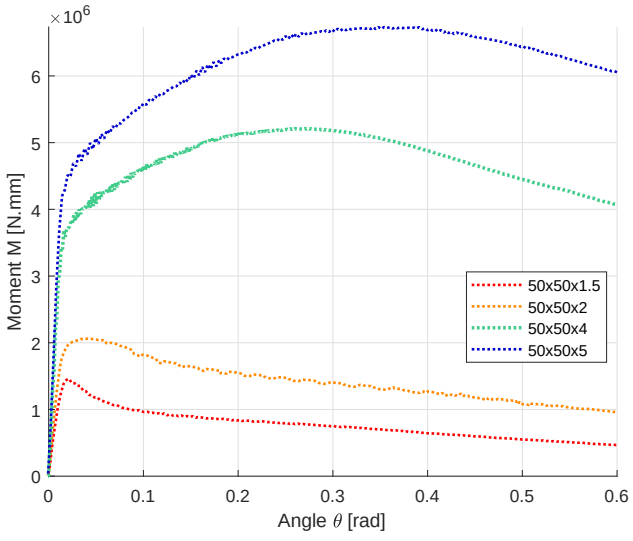

Figure 2: Moment- angle $M-\theta$ curve for different SHS 50x50 with various thicknesses. Results obtained with numerical simulations of a three-point bending test and steel S275.

All the aforementioned limitations are evident when comparing the resulting $M-\theta$ curves of shapes with different thicknesses (see Fig. 2). When a medium-thin-walled, rectangular or square hollow shape is used, the maximum moment is significantly increased (which is expected since the second moment of inertia is also increased); however, a not-so-evident consequence is that θ_m, corresponding to M_m, is no longer negligible. This fact indicates that the collapse does not occur immediately after the elastic portion (which is an assumption for very thin shapes). This phenomenon was also observed by Huang et al. [12] and is explained as the failure mode switches from pure bending collapse to collapse with indentation, or even pure indentation (depending on the length of the shape). An alternate explanation is proposed for medium-thin-walled shapes:

since the yielding does not occur at all points in the through-the-thickness direction at the same time, there is a significant portion of the $M-\theta$ curve with simultaneous elastic and plastic deformations. Thus, the maximum moment is not reached immediately after the load reaches the elastic limit value, instead it happens after most of the points have suffered yielding. The most notable consequence of it being that the energy absorbed before reaching the maximum moment is no longer negligible.

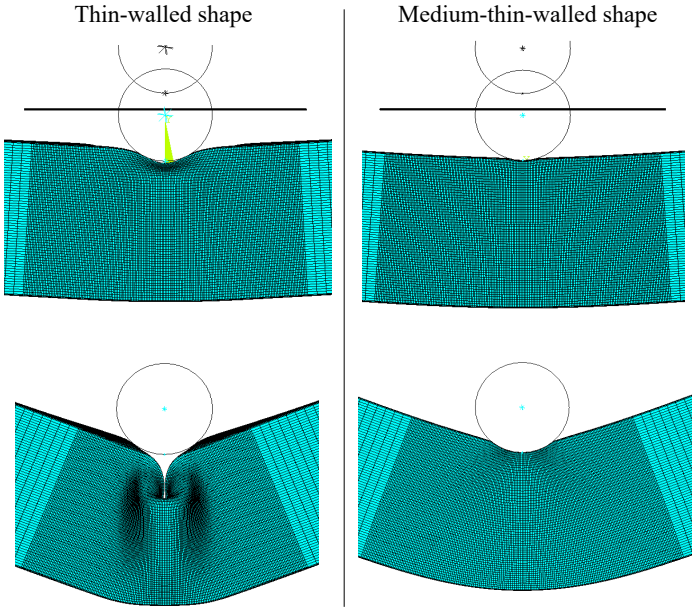

Figure 3: For thin-walled SHS (left) collapse begins with low displacement in the three-point bending test and closely follows Kecman's model; for thicker medium-thin-walled SHS (right), the collapse requires a larger displacement from the force applicator and includes some indentation and subsequently a larger θ_m. Thus, θ_m cannot be neglected with thicker shapes.

2.2. Proposed modifications to the collapse theory

To address the limitations in Kecman's theory for medium-thin-walled shapes, certain modifications are proposed in this section. Kecman's model has already been modified in the past. The first modifications consist of correcting some kinematic incompatibilities, however, these corrections provide little improve-

ments to the results accuracy as shown by Kim and Reid [8]. Other modifications consist of changing some terms of the collapse theory, to include the influence of additional materials, specifically changing the term m_p to a more general m_0, as well as the Eq. 19 to 26 [9]. Other modifications have been made to include the elastic and elastic-plastic regions of the $M - \theta$ curve [12]. However, it was found that some of these approximations seem to work only for certain materials, since they were constructed by fitting experimental results of only one material (e.g. aluminum). In general, a modification to the theory should include all stages of deformation, namely: elastic, elastic-plastic, and collapse (Fig. 3), since θ_m cannot always be approximated to zero. These stages are shown in Fig. 4. These modifications should be able to address most of the aforementioned limitations, evident experimentally in the fact that with larger ratios of t/b, the hinge lines are no longer well defined, as seen both in Figs. 3 and 5.

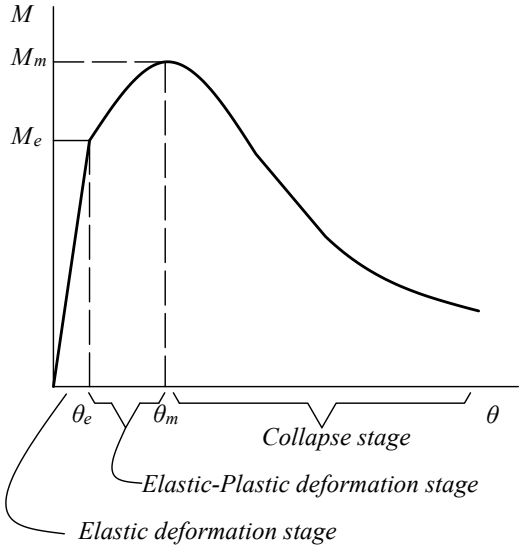

Figure 4: General shape of a $M - \theta$ curve, showing three main stages.

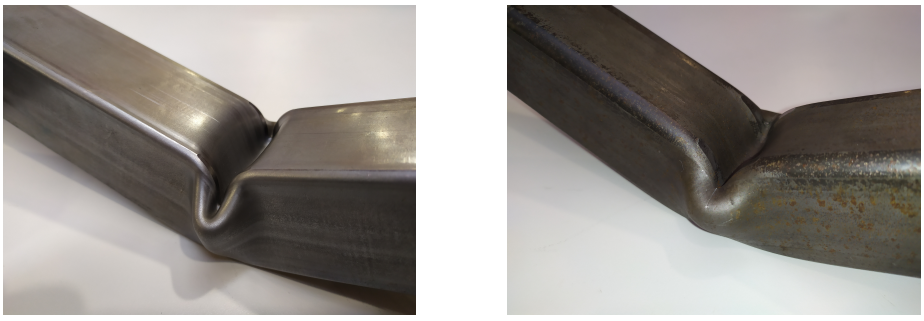

Figure 5: Comparison between collapsed test specimens with $t/b = 0.04$ (left) and $t/b = 0.08$ (right). Notice that the thicker specimen (right) does not show well defined hinge lines, thus a correction is needed.

2.2.1. Elastic deformation stage

The initial stage considers only the effect of elastic deformation, up to the point where plastic deformation starts. The maximum elastic moment M_e and corresponding angular deformation θ_e can be estimated when the normal stress at the top (or bottom) flange of the shape reaches the yield strength. For a beam in the three-point bending test configuration, the following equations from technical mechanics, for a simply supported beam with a concentrated load in the middle, can be used:

$$M_e = 0.9\frac{\sigma_Y(ab^3 - (a-2t)(b-2t)^3)}{6b} \tag{3}$$

$$\theta_e = \frac{3M_e l_s}{Eb^2t(b+3a)} \tag{4}$$

where σ_Y is the yield strength of the material; E is the elasticity modulus; b, a and t are the height, width and thickness of the hollow shape, respectively; and l_s is the span in between supports of the three-point bending test, as shown in Fig. 6.

The elastic deformation zone is then defined as a line between the origin and the elastic limit point (θ_e, M_e). Notice that depending on the thickness of the shape, this expression may sometimes slightly overestimate the value of M_e,

thus the value of 0.9 is introduced to compensate. This seemingly occurs merely because the force applicator tends to initially crush the cross sections directly under it.

2.2.2. Elastic-plastic deformation stage

During the elastic-plastic deformation stage, there are two phenomena occurring simultaneously: there are cross sections with both elastic and plastic deformations, and the zones with plastic strains also endure hardening. This stage typically occurs quickly in thin-walled shapes, but it is significant in medium-thin-walled shapes, as shown in the comparison in Fig. 3. This region can be approximated by a parabola, that passes through the points (θ_e, M_e) and (θ_m, M_m). However, this information is not enough to fully define the parabola. The maximum moment M_m, defined later in the collapse stage, cannot be surpassed, which means that the point (θ_m, M_m) can work as a vertex of the parabola. Since there is no analytical expression for the angle θ_m, it is proposed that its value is obtained by fitting the results from the numerical simulations. The procedure is further detailed in the following section.

2.2.3. Collapse stage and modifications

A comparison for the collapse stage in thin-walled and medium-thin-walled shapes is shown in Fig. 3. The first modification to the original theory was described by Kecman himself. The numerical derivation mentioned in Eq. 1 typically results in extremely high bending moments for very low angles (typically 10 to 20 times than the actual maximum bending moment). Kecman initially attempted to overcome this limitation, by calculating M_m and connecting the point $(0, M_m)$ (neglecting θ_m) to the curve $M - \theta$ with a tangent line. Since this procedure is empirical, later authors usually intersect the $M - \theta$ with an horizontal line that passes through M_m, and thus obtaining θ_m. In this research, it is observed that the initial correction by Kecman can still be used for "medium-thin-walled" SHS and RHS. However, the resulting M_m and θ_m are usually underestimated so further modifications are introduced.

All terms for the energy absorbed during collapse depend on Eq. 2; and in turn, this equation is dependent on the flow stress σ_0. During the formation of the hinge lines, not all points reach the yield stress σ_Y and the flow stress σ_0 at the same time, thus the approximation $\sigma_0 = \sigma_B$, as well as the use of σ_Y are no longer adequate. Wierzbicki and Abramowicz [6, 7] estimated that the nominal flow stress is actually less than the ultimate strength σ_B; whereas Kim and Reid [8] estimated that, depending on σ_{cr} (see Appendix, Eq. 13), the nominal flow stress can be estimated as the average of both σ_Y and σ_B. In this work, an effective yield strength σ_{Ye} and an effective flow stress σ_{0e} are defined based on a linear relationship between σ_Y and σ_B:

$$\sigma_{Ye} = a_e \cdot \sigma_Y + (1 - a_e) \cdot \sigma_B \tag{5}$$

$$\sigma_{0e} = c_e \cdot \sigma_Y + (1 - c_e) \cdot \sigma_B \tag{6}$$

where $0 \leq a_e \leq 1$ and $0 \leq c_e \leq 1$. These factors are in turn dependent on the thickness-to-height ratio t/b for SHS, as well as the height-to-width ratio b/a for RHS. For this work, the reference $M - \theta$ curves are obtained from numerical simulations of the three-point bending test (described in the following section), and each factor is determined from said results as follows:

- a_e: This factor determines the effective yield strength, and is directly responsible for the maximum moment M_m. Thus, only the M_m is used to determine a_e for different t/b proportions for SHS (and b/a for RHS). M_m is obtained through numerical simulations, and the relationship of a_e and t/b and b/a can be fitted from the simulation results for different ratios (see Fig. 12 and 13 in the results section).

- c_e: This factor describes the behavior after the maximum moment is reached, as the Eq. 2 (which is needed for Eqs. 19 to 26) requires the effective flow stress. This value is determined by minimizing the difference between the energy absorbed after collapse from numerical simulations

and the energy absorbed after collapse using the proposed model. Both absorbed energy values are obtained using the area under each curve after M_m is reached.

- θ_m, i.e. the angle where M_m occurs, is obtained with numerical simulations for various values of t/b and b/a. This value is used to "offset" the collapse stage obtained by the original model. The relationship between θ_m and t/b can also be fitted from the numerical results (see Figs. 14 and 15 in the results section).

These factors are calculated and obtained for various calibration sizes of SHS and RHS corresponding to different ratios. These calibration sizes are displayed in Tables 2 and 3. Next, the obtained factors a_e, c_e and θ_m are tested and verified by predicting the complete behavior in SHS and RHS for sizes not used in the calibration. The sizes used to verify the accuracy of the proposed modification are displayed in Tables 4 and 5. Using the factors a_e, c_e and θ_m, the following procedure is proposed to obtain the bending collapse behavior:

Step 1. Determine the maximum collapse moment M_m (see appendix), which depends on factor a_e, which in turn depends on the ratio t/b (and b/a for RHS). Depending on the case, a_e can be determined with a curve fit (SHS) or a surface fit (RHS), both are shown in the next section.

Step 2. Calculate modified Kecman curve, based on factor c_e, and define a tangent line that crosses the point $(0, M_m)$. This corresponds to the original Kecman modification. Depending on the case, c_e can be determined with a curve fit (SHS) or a surface fit (RHS), both are shown in the next section.

Step 3. Offset the resulting curve horizontally, until the top of the curve reaches the point (θ_m, M_m). By offsetting the curve, the elastic and elastic-plastic stages can be included. Depending on the case, θ_m can be determined with a curve fit (SHS) or a surface fit (RHS), both are shown in the next section.

Step 4. Connect the origin with point (θ_e, M_e) with a line, which describes the elastic stage.

Step 5. Connect the point (θ_e, M_e) with point (θ_m, M_m) with a parabola, with vertex at (θ_m, M_m). This parabola describes the elastic-plastic stage.

It should be noted that even though we propose that the values of a_e, c_e and θ_m should be obtained by numerical simulations (validated through experimental tests), they could also be determined using experimental tests if different shape sizes are available.

3. Procedure

3.1. Experimental test setup

As mentioned above, there are two alternatives to obtain a bending collapse (either with experiments or simulations): a cantilever test and a three-point bending test; the latter being the most commonly used in recent literature and simpler to reproduce. In this work, a three-point bending test is performed of different hollow shapes, with different values of ratios t/b, but maintaining a ratio of $l_s/b = 10$ to ensure bending collapse with minimum indentation. The scheme in Fig 6 is used as the base for the experimental setup, seen in Fig. 7. The tested sizes are shown in Table 1. Since the hollow shapes are manufactured by welding, the weld is always kept in the bottom part (in contact with the supports), so that it is subjected to traction along the weld, thus limiting its possible influence on the collapse behavior.

For all tests, the force applicator consists of a cylinder with 30 mm diameter, connected to a force sensor capable of measuring up to 200 kN. Two pairs of support cylinders have been used. The first pair consist on the supports shown in Fig. 7, which also have a diameter of 30 mm. However, for the tests of the specimens SHS50x50x2 and SHS50x50x4, a pair of supports with 48 mm of diameter are used, which have a stronger base. The reason for the switch is the fact that the larger shapes required a larger l_s to obtain bending collapse, and the lateral force that the supports must endure is larger than the

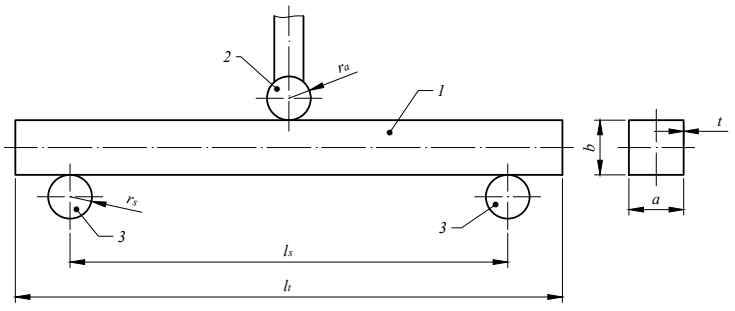

Figure 6: Three-point bending test scheme. 1: test specimen (RHS or SHS), 2: force applicator, 3: supports

maximum lateral force that the first pair of supports could withstand. All tests are performed with a velocity of 1 mm/s.

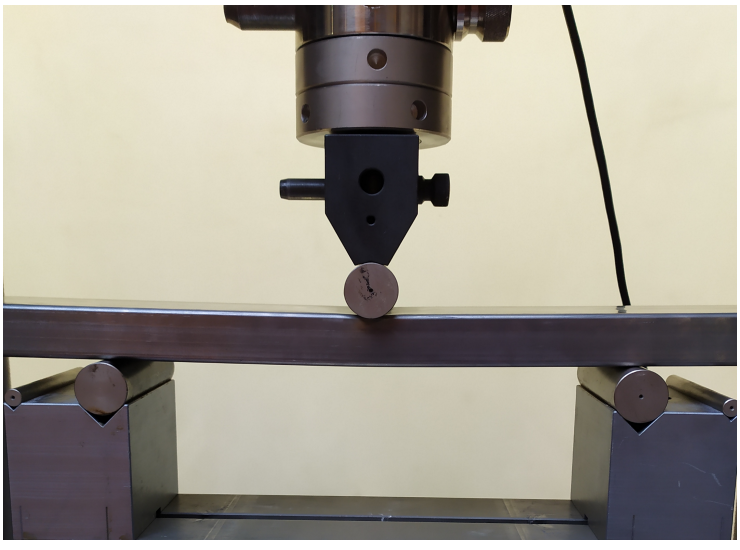

Figure 7: Experimental setup for the three-point test scheme.

Material properties are extracted from coupons obtained from the sides of the hollow shapes. For each shape size, two coupons are obtained. The geometry of the test coupons is defined according to standard ASTM A370. The resulting engineering stress and strain curves are shown in Fig. 8.

It is worth noting that one of the resulting stress and strain curves shows an

Table 1: Dimensions of tested specimens.

Nomenclature	height b (mm)	width a (mm)	thickness t (mm)	ratio t/b (-)	Span l_s (mm)
SHS25x25x1.5	25	25	1.5	0.06	250
SHS25x25x2	25	25	2	0.08	250
RHS30x80x1.5	30	80	1.5	0.05	300
SHS50x50x2	50	50	2	0.04	475
SHS50x50x4	50	50	4	0.08	475

elastic-perfectly plastic behavior, however, the other coupons do exhibit plastic hardening. Even when all shapes are sold as S275, they do not have the same actual values for yield and ultimate strengths although they satisfy the minimum requirements to be classified as such. This is most likely due to the manufacturing process for each shape. It should be noted, that the forming process of hollow shapes requires plastic deformations of the base material, which increases both the yield and ultimate strengths.

3.2. Numerical simulation setup

The scheme in Fig. 6 is used as a base to build the numerical model, seen in Fig. 9. The FEM model is built in Ansys Classic (APDL) 2019R1, with the dimensions and material properties as input parameters, which are changed for the different sizes and material properties. The parameters are defined in Matlab, where a script modifies the APDL input files. Once modified, they are sent to Ansys via the toolbox Ansys AAS (Ansys as a server) [31]. The results of each simulation are then exported and can be read in Matlab for further post-processing. The FEM model consists of 8-node brick elements with 3 elements in the through-the-thickness direction of the shapes. Furthermore, the mesh is refined near the contact zone of the force applicator, with elements of 1 mm of length in the longitudinal direction. The top and bottom faces near the force applicator and supports are covered with penalty-based contact elements.

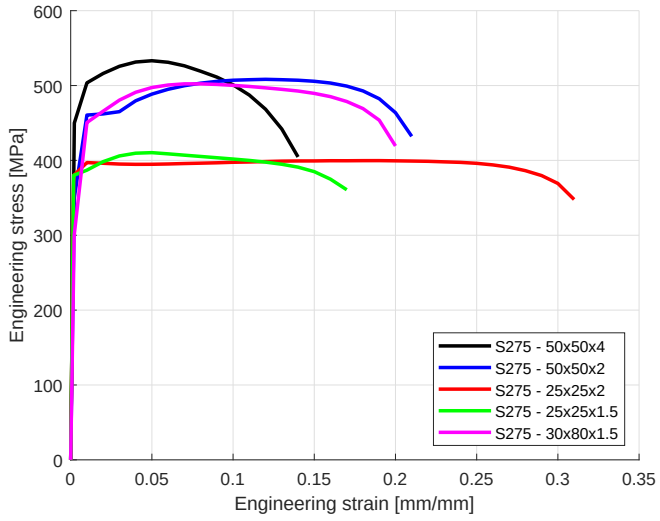

Figure 8: Engineering stress-strain curves from the coupons extracted from the test specimens. Averaged results. All samples are rated as S275.

The force applicator and the supports are modeled using one target element each, which is shaped as a hollow rigid cylinder with its movement constrained through a pilot node at its axis. This configuration offers adequately accurate results, with less elements and allows the boundary conditions to be set on pilot nodes at the center of the cylinders. The results do not differ significantly from previous simulations, where the supports and force applicator were meshed with a finer mesh and numerous elements in the cylinders (and longer simulation time). Since the focus of the research is on the collapse of the hollow shapes, the cylinders are modeled as rigid bodies. Pilot nodes are also added at both ends of the test specimen, to restrict the average movement out of the bending plane, without restricting each particular node to move in the out-of-plane direction. These constraints are added for stability and produce near-zero reaction forces. All models have up to 205000 nodes and up to 162000 elements. The supports are initially in contact with the SHS (or RHS), and the force applicator is initially located with an offset of 5 mm above the top face of the test specimen, so there is no initial contact. The model and its details can be seen in Fig. 9.

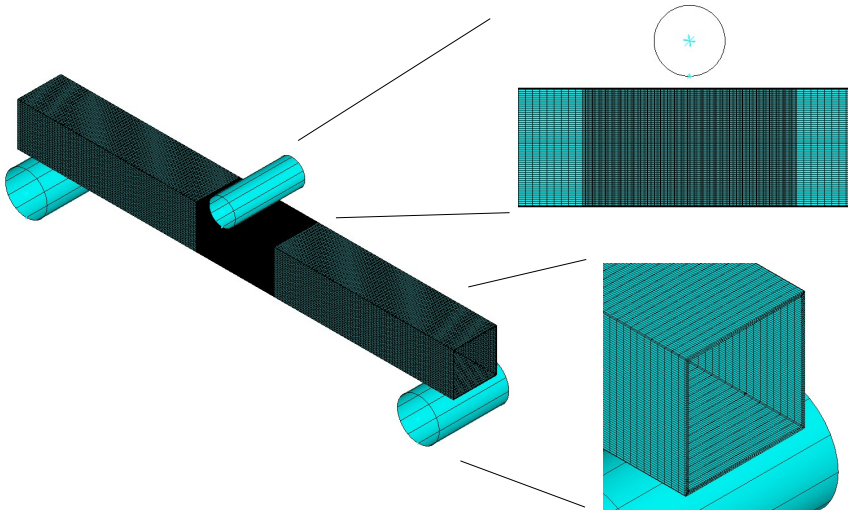

Figure 9: Numerical model for the bending collapse. Details of the numerical model: Top right: force applicator in the initial position and refinement of the mesh in the collapse portion. bottom right: Mapped meshing in the through-the-thickness direction.

The model also includes fillets with radii that depend on the dimensions of the shape, according to standards EN 10219 and EN 10305. Authors such as Zhang et al.[32] have found that the presence fillets may have a significant influence in the maximum moment and later response. It has been theorized by the aforementioned author, that the fillets act as triggers for the collapse. In fact, the hollow shape standards EN 10219 and EN 10305 establish a range of acceptable fillet radii according to the size. Thus, fillets are included in the geometry for the FEM simulations. It is worth noting that their influence appears to be present only on the maximum moment, not in the collapse stage itself, thus its influence is included in a_e. The theoretical model (seen in Fig. 1) does not take the fillets into account. It can be argued that since the arc length of the fillets is rather small when compared with the height or width of the shape,

its influence on the collapse stage is negligible.

The velocity of load application is also important since the response and $M - \theta$ curves change for static and impact loads. Dynamic response can also be approximated from the static loading, by multiplying the static response curve by a factor K_d that depends on the material, in case of steel $K_d = 1.2$ [25]. Thus, only a quasi-static test scenario is performed. The selected force applicator velocity is set to 1 mm/s. The SHS and RHS are made of steel S275. A linear elastic model is used for the elastic portion of the stress-strain curve; since plastic deformations are expected, a piecewise plastic hardening rule is also used. The plastic hardening rule is based on the true-stress and true-strain curve obtained from Fig. 8 (for the validation of the numerical model) and from [33] (for the calculation of different sizes).

The main outputs of the simulation are the imposed vertical displacement u_y and the reaction force on the pilot node of the force applicator f_y. These results cannot be used to make a direct comparison between the numerical simulations and the proposed analytical model; since the output of the latter is a $M - \theta$ curve instead of a $f_y - u_y$ curve. These results are also highly dependent on the length between supports l_s (seen in Fig. 6). In order to make a comparison between the two approaches, the internal bending moment from the numerical simulation is determined using the section method (from technical mechanics) and assuming a quasi-static process, both for a simply supported beam (Eq. 7). On the other hand, the angle θ can be approximated by a geometric relationship (Eq. 8), assuming that the bending angle along the beam is negligible and the center portion of the beam acts as a hinge:

$$M = \frac{f_y l_s}{4} \tag{7}$$

$$\theta = 2 \arctan\left(\frac{2u_y}{l_s}\right) \tag{8}$$

3.3. Results and validation of the numerical simulation

Using the results from the three-point bending experiment, as well as the mechanical properties obtained from the coupons, the accuracy of the numerical model can be evaluated and the model validated. It is important to note that the material properties are not the same for every size, and the corresponding properties are taken from Fig. 8. The model includes characteristics such as fillets (average fillet radius) and can be used for materials with either perfectly plastic behavior or plastic hardening. The comparison of the results is performed by using the $M - \theta$ curves as shown in Fig. 10.

The numerical model seems to adequately reproduce the experimental results. Each experimental test was performed three times, except for the 50x50x2 shape. For this last one, the test was also performed with the longitudinal weld in the lateral and top positions. No significant difference or apparent influence of the weld on the collapse behavior or the maximum moment has been found.

3.4. Dimensions for the test specimens in the numerical simulations

Different dimensions are chosen to obtain $M-\theta$ curves and fit the results for the parameters a_e, c_e and θ_m. The results are analyzed in function of certain ratios for the SHS and RHS. The thickness-to-height ratio t/b is used to address the relative thickness of the test specimen, for both SHS and RHS. The height-to-width ratio b/a is also used to address the influence of the width of the test specimen. In order to better understand the meaning of the last factor, the following visual aid is provided in Fig. 11.

To guarantee a bending collapse failure instead of indentation, a minimum proportion of $l_s/b \geq 9$ is chosen [12]; simulations were also run to verify this value. The length $l = 500$ mm is selected to guarantee bending collapse for all tested specimens, which corresponds to $l_s = 450$ mm, giving 50 mm to both extremes. This means that a maximum height b of 50 mm is used. Different thicknesses for various heights are then chosen to obtain t/b ratios in the range of $0.03 \leq t/b \leq 0.1$, which correspond to the medium-thin-walled shapes, the

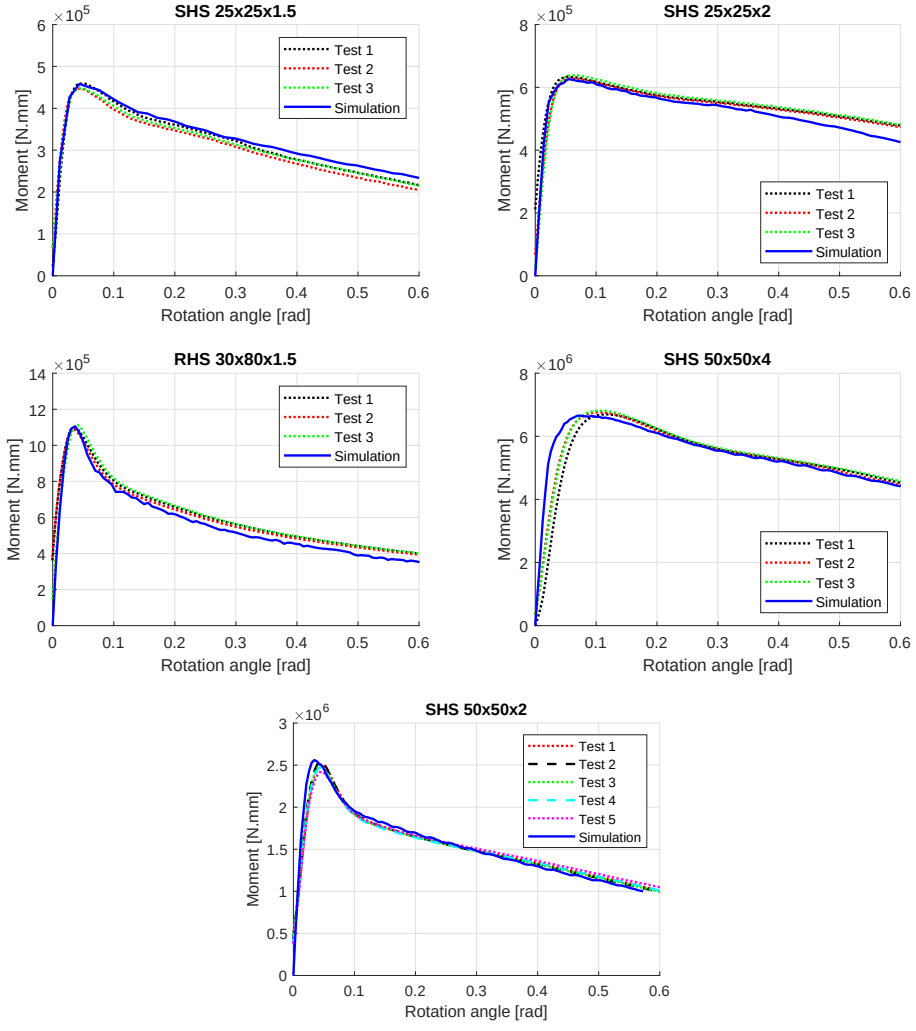

Figure 10: Comparison of the experimental results and numerical results with different shape sizes.

focus of this study. These values are detailed in Table 2.

It is also worth noting, that the length between supports has a minor influence on θ_m, as long as bending collapse is guaranteed. Bending collapse occurs due to the influence of only the bending moment in the beam, thus the

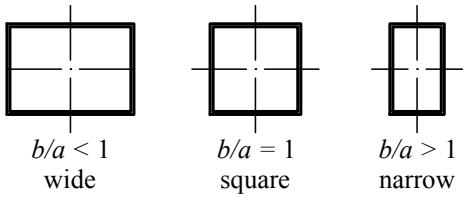

Figure 11: Visual aid showing wide and narrow rectangular hollow shapes.

maximum moment should not be significantly affected by different lengths l_s. However, θ is determined through an approximation (recall Eq. 8) which depends on u_y; thus, larger values of l_s give larger u_y and, in turn, make θ grow. The authors did not find a significant difference in the maximum moment when l_s is increased, and only a slight increase in θ_m. It should be noted, however, that in case that a more compliant material was used (e.g. aluminum), a larger increase should be expected.

Table 2: SHS dimensions for calibration- all taken from standard EN 10305.

SHS ($b \times b \times t$)	t/b	Thickness
25x25x1.5	0.06	medium-thin
25x25x2	0.08	medium-thin
30x30x2	0.067	medium-thin
40x40x1.5	0.038	medium-thin
40x40x2	0.05	medium-thin
50x50x1.5	0.03	thin
50x50x2	0.04	medium-thin
50x50x4	0.08	medium-thin
50x50x5	0.1	medium-thin

For the RHS, the standard EN 10305 and material S275 are also used. The chosen dimensions must satisfy the same conditions for the SHS: cover a range of values of t/b. Moreover, the influence of the ratio b/a also has to be analyzed.

There are various combinations of t/b and b/a. In order to avoid analyzing each possible combination of ratios and having to deal with an excessive sample size and computational time, Latin-hypercube sampling is used to obtain a reduced sample size. However, even when there are numerous possible combinations (around 73 in the considered range), only around 8 different levels are identified based on the commercially available sizes. Introducing more levels is not feasible, since the resulting Latin hypercube levels must be rounded to the nearest available commercial size. This may result in repeating values, and defeating the purpose of the Latin-hypercube sampling. The selected sizes are shown in Table 3. Note that some levels are inevitably repeated.

Table 3: RHS dimensions for calibration- all taken from standard EN 10305.

RHS ($b \times a \times t$)	t/b	b/a
45x45x1.5	0.033	1
50x80x2	0.04	0.625
50x30x2.5	0.05	1.667
35x70x2	0.057	0.5
40x60x2.5	0.0625	0.667
30x15x2	0.0667	2
40x60x3	0.075	0.667
40x27x3	0.075	1.48

The results obtained with the dimensions selected in Tables 2 and 3 are used to calibrate the modifications of the theoretical model, i.e. factors a_e, c_e and θ_m. Numerical simulations are also run on the dimensions of the commercially available shapes, shown in Tables 4 and 5, to compare the accuracy of the proposed modifications.

The material properties for the numerical simulations used for the different shapes have a great influence on the results. Even when they are made from the same steel, the manufacturing process has a large influence on the final yield and ultimate strengths as discussed before. To ensure a proper calculation tensile

Table 4: SHS dimensions for testing- all taken from standard EN 10305.

SHS ($b \times b \times t$)	t/b
30x30x1.5	0.05
35x35x2	0.057
40x40x3	0.075
45x45x2	0.044
45x45x3	0.067

Table 5: RHS dimensions for testing- all taken from standard EN 10305.

RHS ($b \times a \times t$)	t/b	b/a
30x50x2	0.067	0.6
40x20x2	0.05	2
40x60x4	0.1	0.667
40x27x1.5	0.038	1.481
50x30x2	0.04	1.667
50x70x2	0.04	0.714
50x100x4	0.08	0.5

tests should be carried out first. However, performing them defeats the purpose of fast and accurate calculations of the maximum bending moment at the early stages of design. There is also the possibility that the properties change from different suppliers. Thus, the calculations of factors a_e, θ_m, and c_e are carried out using the nominal properties of steel S275, which are shown in Table 6.

4. Results and discussion

In this section, the results obtained with numerical simulations are used to approximate the relationship between the factors a_e, c_e, and θ_m for the various ratios t/b and b/a. The obtained fits are then tested with sizes not used in the calibration. Furthermore, the resulting $M - \theta$ curves obtained by the proposed

Table 6: Mechanical properties of S275, taken from [33].

Property	Value	Units
Young modulus	200	GPa
Poisson ratio	0.3	-
Minimum yield strength σ_Y	275	MPa
Ultimate strength σ_B	480	MPa

model are compared to the numerical simulation to test its accuracy, and to Kecman's original theory to verify the improvement for medium-thin-walled shapes.

4.1. Parameters for the proposed modification of the collapse stage

4.1.1. Effective yield stress factor a_e

The resulting a_e curve for SHS shows a clear tendency downwards with increasing t/b, as shown in Fig. 12. This means that the effective yield strength increases with larger ratios of t/b (lower a_e translates into a higher σ_{Ye}). However, the relationship between a_e and t/b is not linear. A polynomial (3rd degree) fit is proposed, obtaining the following relationship:

$$a_e(t/b) = 1472(t/b)^3 - 192.9(t/b)^2 - 7.015(t/b) + 1.357 \tag{9}$$

The goodness of the fit is measured through R-square, resulting in 0.9934; and a SSE, resulting in 0.004387. The polynomial fit can be seen in Fig. 12.

It is worth noting that values of a_e larger than one, would mean that there is collapse before yielding, which may occur with very thin-walled shapes. Also, Kecman's models consider that $a_e = 1$ and gives good results for thin-walled shapes. Larger values of t/b mean that the profile is not that thin anymore, and the prediction of the maximum moment is not accurate without the factor a_e. For $t/b > 0.1$, a_e seems to converge at around 0.2 for SHS.

As for the RHS, the factor a_e tends to decrease with thicker shapes, which indicates that yielding in the through-the-thickness direction does not occur

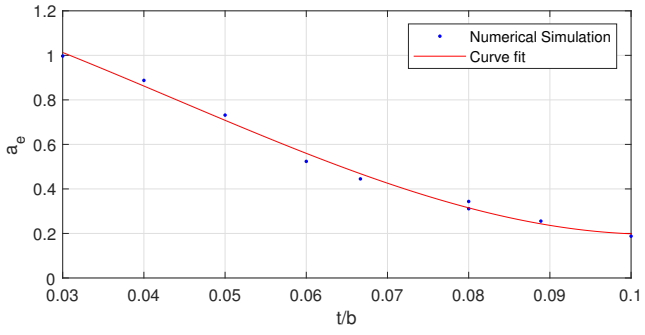

Figure 12: Relationship between a_e and t/b.

at all points at the same time. Moreover, the ratio b/a also influences the behavior of a_e significantly. Lower values of b/a tend to increase a_e, meaning that "narrow" RHS tend to collapse later than "wider" RHS of the same height b. This behavior can be explained by the fact that, for a set height b, a larger a (ergo lower b/a) makes the hollow shape also relatively thin-walled in the direction perpendicular to the bending plane, making it more prone to collapse, with faster formation of hinge lines. The relationship between a_e vs t/b and b/a is shown in Fig. 13.

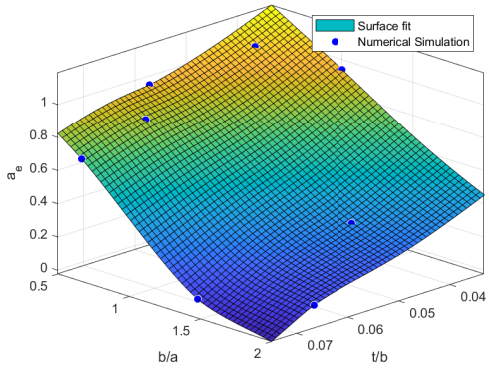

Figure 13: Surface of the relationship between a_e and ratios t/b and b/a obtained through a thin-plate spline interpolation.

4.1.2. Angle θ_m at which M_m occurs

Similarly, the angle θ_m can also be related to the ratio t/b as shown in Fig. 14. It is found that for low values of t/b or very thin-walled shapes, this angle is almost zero. This fact agrees with the works by previous authors, such as Kecman [4] and Kim [8], who consider that this angle is negligible. However, when the thickness increases, the angle θ_m grows as well and tends to reach the value of around 0.35 radians. Due to the shape of the simulation points, a sigmoid fit is proposed as follows:

$$\theta_m(t/b) = \frac{0.3484}{1 + \exp\left(-\dfrac{t/b - 0.05972}{0.009577}\right)} \tag{10}$$

The sigmoid-like fit achieves an R-square of 0.9763 and a SSE of 0.003257.

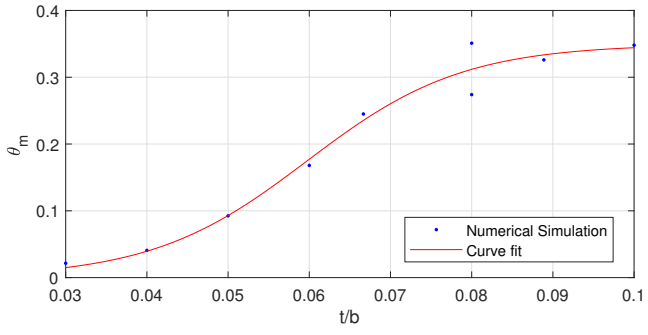

Figure 14: Relationship between θ_m and t/b.

The behavior of the angle θ_m is explored for the RHS cases as well, and a similar behavior of the one shown in Fig. 14 is found. It is observed once again that thicker shapes tend to increase θ_m significantly. However, this increase depends also on the ratio b/a as narrow beams tend to increase θ_m even more, as shown in Fig. 15. This behavior can also be explained. For larger a lengths, or wider RHS, the shape becomes thinner in the horizontal direction (perpendicular to the bending plane) and, similarly to a_e in Fig. 13, the shape becomes more susceptible collapse, as hinge lines form rapidly with ease.

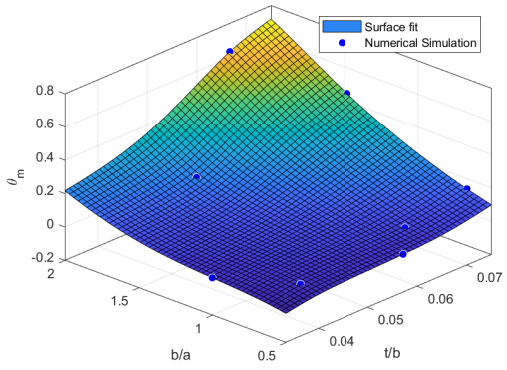

Figure 15: Surface of the relationship between θ_m and ratios t/b and b/a obtained through a thin-plate spline interpolation.

4.1.3. Effective flow stress factor c_e

In contrast to a_e, c_e and t/b do not seem to have a clear relationship. However, many simulations show that $0 \leq c_e \leq 0.5$ (Fig. 16), meaning that the effective flow stress lies between $0.5(\sigma_Y + \sigma_B)$ and σ_B, which seems to agree with previous authors such as Kim and Reid [8], and Abramowicz et al. [34]. There are some points with very high values of c_e, meaning that there is a low value of σ_{0e}. This behavior can be explained by showing a second relationship, between c_e, t/b and b/l_s (see Fig. 17). It can be seen that the three apparent outliers with c_e near 1 are also those with a high ratio b/l_s, which translates into shorter test specimen and in turn some indentation. When using short specimens $b/l_s > 0.125$ (or $l_s/b < 8$) there is a significant amount of indentation in the test specimen [12].

When including the ratio b/a in the comparison (for RHS), more insight into the factor c_e can be extracted, as shown in Fig. 18. In general, thin and wide shapes tend to have a slightly higher value of c_e, however, this value lies in the 0.4 to 0.6 range. This result, as the one for SHS, agrees with the assumptions by previous authors who make fixed approximations for the nominal flow stress. For narrow and thicker shapes, c_e tends to be also slightly larger, meaning that

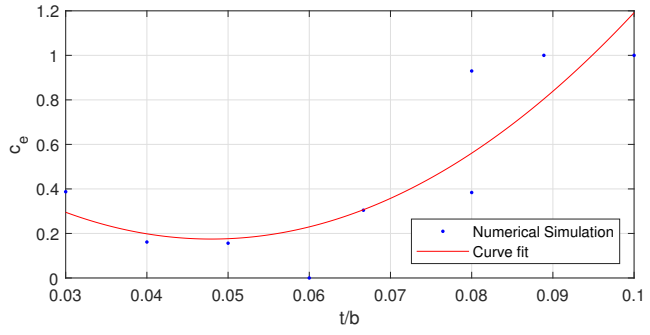

Figure 16: Relationship between c_e and t/b.

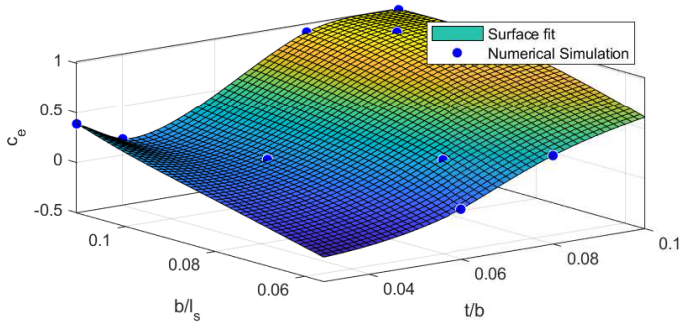

Figure 17: Relationship between c_e and t/b and b/l_s using a thin-plate spline interpolation.

the flow stress is actually lowered. An explanation for this behavior is proposed as the cross section under the force applicator tends to be crushed, and the failure mode is actually collapse and indentation (recall Fig. 3). This means that points near the cross section actually require less load to reach the flow stress, since they are already deformed due to the indentation.

4.2. Verification of the parameters with test sizes

All parameters a_e, c_e and θ_m are calculated using the curve and surface fits shown above and used to obtain the corresponding $M - \theta$ curves, which are then compared to numerical simulations. The accuracy of the prediction of the original model is computed as well to determine which model is better at predicting the collapse behavior for thin and medium-thin-walled shapes.

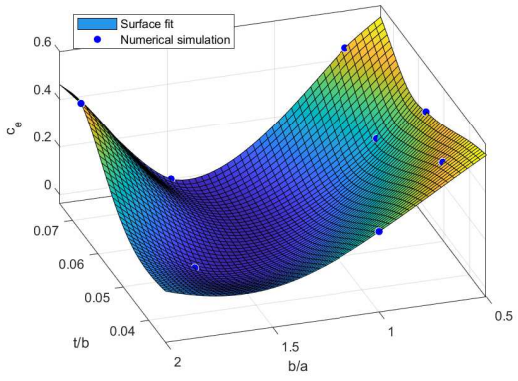

Figure 18: Surface of the relationship between c_e and ratios t/b and b/a obtained through a thin-plate spline interpolation.

The accuracy is measured using an error percentage, with the numerical model results as reference, as indicated in Eq. 11 and 12.

$$Error = \frac{|M_{numerical} - M_{proposed}|}{M_{numerical}} \times 100\% \tag{11}$$

$$Error = \frac{|M_{numerical} - M_{original}|}{M_{numerical}} \times 100\% \tag{12}$$

4.2.1. Square hollow shapes

The comparison $M - \theta$ curves for SHS using the approximations for a_e, c_e, and θ_m are shown in Fig. 19. The obtained curves show that for most cases the error for the proposed analytical model is kept at less than 5% most of the time, with few exceptions in points where the error grows as large as 10%. In contrast, the error for the Kecman original model can be as large as 20% and in some cases up to 30%; with both errors tending to decrease for large values of θ. In most cases, the largest error occurs at θ_m for the original model which shows a poor prediction for M_m. Factor a_e and θ_m seem to almost completely overcome this problem, for the proposed model. Factor c_e apparently reduces the error for $\theta > \theta_m$. There is also apparently an extremely large error for $\theta = 0$. This apparent large error occurs mainly because the original model does

not predict the elastic behavior. For all SHS examined, the proposed model with modifications can estimate the numerical prediction with better accuracy than the original theory. This improvement is more noticeable with the relatively thicker shapes SHS40x40x3 and SHS45x45x3, which confirms the capacity of the proposed model to predict the maximum moment and collapse behavior for "medium-thin-walled" shapes.

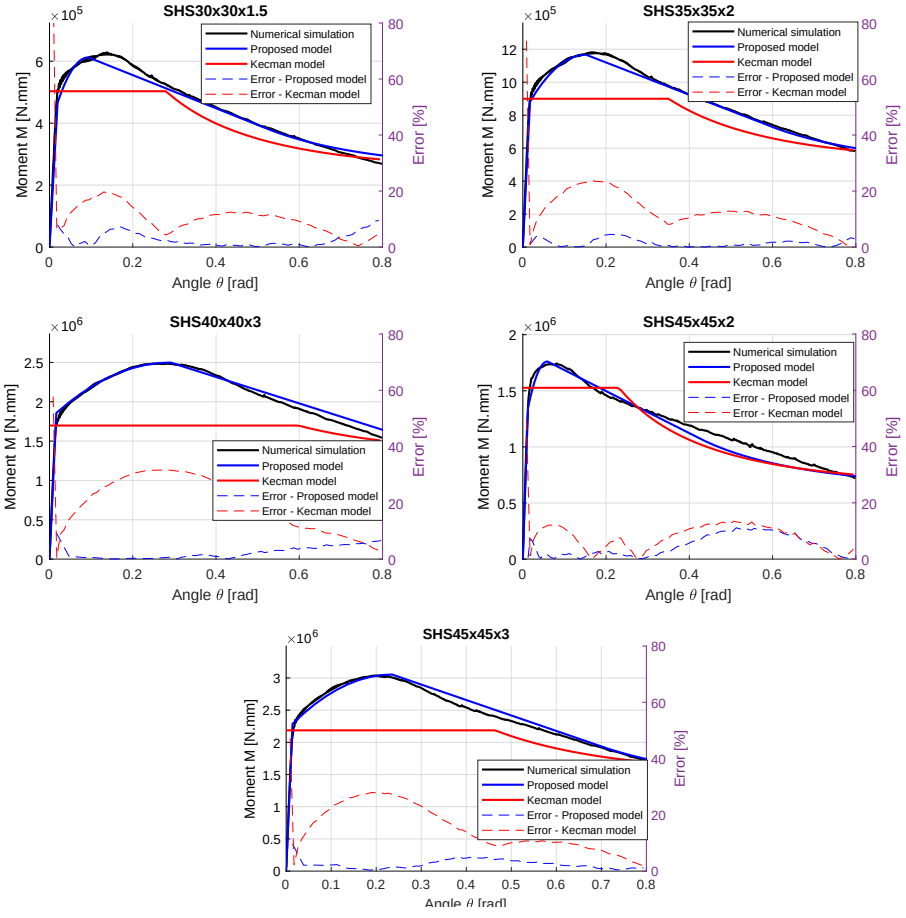

Figure 19: Comparison between the $M - \theta$ curves for the various SHS tested.

Another important comparison is the energy absorbed by each approach, which can be calculated by the area under each one of the aforementioned curves. The energy absorbed or work results for each case is detailed in Table

7 along with its error with respect to the numerical simulation result. These results seem to also indicate that the proposed corrections are able to reproduce the results obtained by numerical simulations with a better accuracy than the original model. The largest error in Table 7 for the proposed approach reaches 3.98%, whereas the highest error for the original model reaches 20.57%, which corresponds to shape with highest t/b ratio. On the other hand, the shape where the original model has the lowest error is also the one with the lowest ratio t/b. This further confirms that the introduced parameters are useful in predicting not only the maximum load, but the energy absorbed as well.

Table 7: Comparison between the energy absorbed (area under the curve) calculated by each method for the SHS.

Size	Numerical simulation	Theoretical (proposed)	Theoretical (original)	Error (proposed)	Error (original)
30x30x1.5	356.66 J	351.34 J	322.75 J	1.49%	9.50%
35x35x2	717.41 J	705.635 J	624.26 J	1.64%	12.98%
40x40x3	1671.06 J	1691.01 J	1327.34 J	1.19%	20.57%
45x45x2	959.36 J	921.19 J	907.08 J	3.98%	5.44%
45x45x3	1946.45 J	1966.68 J	1638.32 J	1.04%	15.83%

4.2.2. Rectangular hollow shapes

A similar analysis is performed for the RHS using the corresponding surface fits and is shown in Fig. 20. The approximation for RHS seems to generate larger errors than the SHS, reaching 10% and, in one case, up to 30 % for the proposed model, and around 30% for the original model. The cases that display larger errors seem to be those where the maximum moment or M_m occurs at a "plateau" and tends to overestimate θ_m, meaning that the proposed modification still has some trouble at predicting where this load occurs. Furthermore, the error seems to oscillate in some scenarios. This oscillation occurs because c_e is obtained by matching the energy absorbed (area under the curve) using the

numerical model after the maximum load is reached, thus it tries to compensate the areas under the curve.

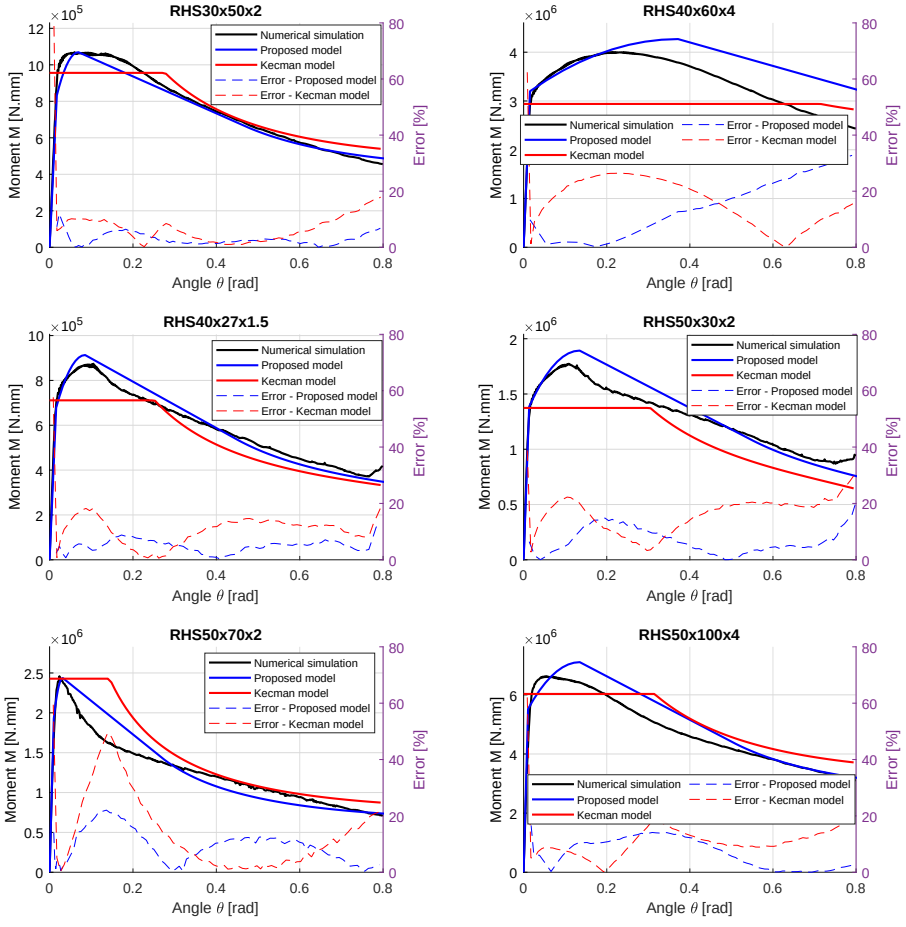

Figure 20: Comparison between the $M - \theta$ curves for the various RHS tested.

It is important to notice that for shapes with low ratios of t/b (thin-walls) and low ratios of b/a (wide), both predictions of the maximum moment (proposed model with modifications and Kecman's) provide almost the same value of M_m. However, the proposed model shows better performance at predicting the maximum moment in all cases. The original model also shows deficiencies

when making predictions for narrow shapes. For instance, two positions for the same shape RHS30x50x2 and RHS50x30x2 are tested. In both cases, the prediction by the proposed model offers a better approximation of the numerical curve but the error for the original model significantly grows when this shape is switched from RHS30x50x2 to RHS50x30x2. This last comparison is important, since it gives insight into the importance of a ratio of thickness and width t/a. However, even when this parameter is not directly investigated, its influence is indirectly included and taken into account in the surface fits for RHS.

Similarly as with the SHS, the area under each curve of each RHS verification case is calculated and shown in Table 8. In general, the proposed model seems to predict thee area under the curve better than the original model; however, there are some cases with apparent exceptions. The first apparent exception is the case where the original model predicts the area under the curve with less error than the proposed model, precisely RHS 30x50x2. It is worth noting that the difference between errors is almost negligible (2.89% to 1.65%) and the proposed model has a better prediction for the maximum moment. The second exception occurs with RHS 40x60x4, where both errors are larger than 10%. This large error is due to an overestimation of θ_m for these dimensions, most likely due to M_m occurring at a "plateau", and not at an exact point.

4.2.3. Comparison with experimental results

Another important observation can be made when comparing the experimental test results with those from the proposed model. Four sets of results are compared against the experimental curves in Fig. 21: 1) the proposed model with the actual mechanical properties and real θ_m (extracted from tensile tests in Fig. 8), 2) the proposed model with the nominal mechanical properties (from Table 6), 3) the original Kecman model calculated using the nominal mechanical properties, and 4) the original Kecman model using the actual mechanical properties. The goal of this comparison is to verify the capabilities of the proposed model to predict the actual $M - \theta$ curves based on the nominal mechan-

Table 8: Comparison between the energy absorbed (area under the curve) calculated by each method for the RHS.

Size	Numerical simulation	Theoretical (proposed)	Theoretical (original)	Error (proposed)	Error (original)
30x50x2	603.29 J	585.81 J	613.23 J	2.89%	1.65%
40x20x2	829.68 J	862.05 J	498.52 J	3.90%	39.9%
40x27x1.5	471.48 J	472.64 J	427.50	0.24%	9.32%
40x60x4	2701.53 J	3022.72 J	2329.42 J	11.89%	13.77%
50x30x2	1024.15 J	1059.39 J	872.18 J	3.44%	14.84%
50x70x2	1004.79 J	1024.39 J	1168.79 J	1.95%	16.32%
50x100x4	3794.85 J	4049.37 J	4055.56 J	6.70%	6.87%

ical properties, as well as to check its accuracy when using the experimental data. The most evident improvement of the proposed model when compared to the Kecman model is, once again, the prediction of M_m, even when using the nominal mechanical properties. This prediction is further improved when the experimental data is used. It should be noted, that this improvement is more noticeable with thicker shapes (SHS25x25x2 and SHS50x50x4). It should also be noted that for the thinner shapes such as (SHS 50x50x2 and RHS30x80x1.5), all predictions seem to agree, which means that the proposed model also works with thin-walled shapes. However, the model apparently still lacks the ability to adequately determine θ_m with nominal material data. The authors theorize that the origin of this difference comes from the strain at which the ultimate stress occurs in the material model (probably due to loss of ductility in during forming), which directly affects how "soon" the maximum moment occurs. The material model used for simulations and posterior calculations does not take into account the loss of ductility from manufacturing, which cannot be known without a tensile test. However, in the early stages of design, having a better prediction with nominal data is of great importance.

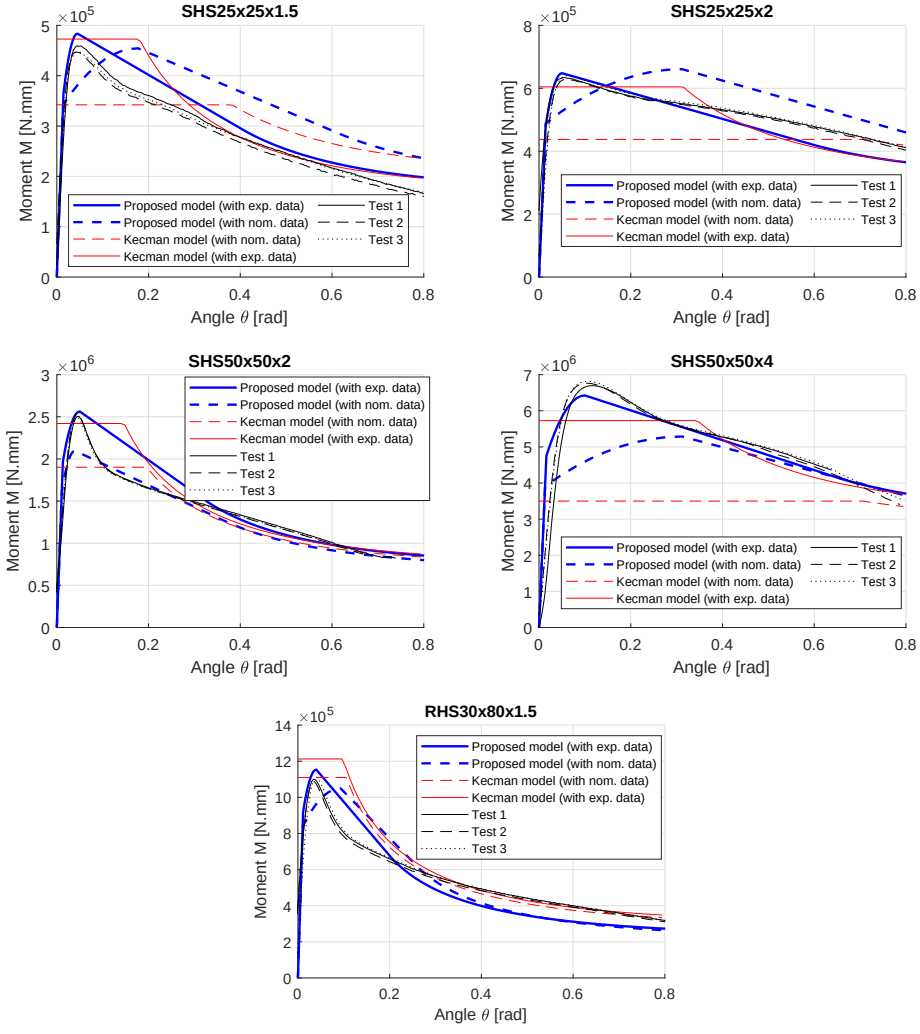

Figure 21: Comparison between the experimental and proposed theoretical models, using the nominal properties for S275.

5. Conclusions

570 A modified approach to calculate the maximum moment and collapse behavior, for steel SHS and RHS is proposed. The proposed modification is mostly based on Kecman's theory and serves to includes the so-called "medium-thin-walled" shapes, commercially available by steel distributors, and widely used in

many industries, such as the automotive industry when constructing bus structures. The bending collapse behavior of the thinner shapes can be described by Kecman's original theory with acceptable accuracy. However, the behavior of thicker or "medium-thin-walled" shapes is better described when including the proposed modifications. The thickness is found not to be the issue, but the thickness relative to the height of the hollow shape, or thickness-to-height ratio t/b. The influence of the width ratio b/a is also explored as well for RHS. It is found that larger values of b/a, or narrower shapes, tend to increase the load required for bending collapse. Also, the thicker and narrower a hollow profile is, the larger θ_m grows. This last observation is of major importance, since many of the previous works consider that, the behavior previous to the collapse, along with θ_m, is negligible, which is not true for the sizes evaluated in this study.

The reasons for which the original Kecman theory fails to identify the maximum load and collapse behavior in "medium-thin-walled" hollow shapes has also been explored. The main reason is that apparently, due to the larger relative thickness t/b, not all points in the through-the-thickness direction of the cross section suffer yielding at the same time, and a larger load is required to completely form the corresponding hinge lines. This fact has three major implications: (1) First, the maximum bending moment is significantly increased. (2) Since the rest of the beam is still deforming until the real maximum bending moment is reached, θ_m also increases, meaning that the behavior previous to the collapse, namely the elastic-plastic stage (see Fig. 4), is no longer negligible. (3) Hinge lines can no longer be clearly defined (recall Fig. 5), and thus the kinematic incompatibilities in the original model, found by some authors such as Kim and Reid [8], may play a larger role. The limitation of the original model is addressed by including two parameters a_e, c_e, which are used to determine an effective yield stress σ_{Ye}, and effective flow stress σ_{0e}, respectively; as well as a prediction for the angle θ_m. All three parameters are dependent on the ratios t/b and b/a. In general, the parameters seem to provide better predictions for the SHS than for the RHS. However, this may be due to the fact that there are

relatively less sampling points for RHS. Even considering this limitation, the inclusion of parameters a_e, c_e and θ_m seems to significantly improve, in most cases, the predictions for both SHS and RHS. This improvement is far more noticeable in the prediction for M_m through a_e, which indicates than an alternative for factor c_e would be useful.

An important remark is that the proposed model can offer improvements in the approximation of a real $M-\theta$ curve. The results obtained with the nominal material data could be considered as a "fast" approximation of the actual curve, as it does not require experimental data fed. In Fig. 21, it can be seen that the results offered by the proposed model, even when using the nominal data, are improved when compared to the original model. The proposed model can further improve its prediction if the experimental data is provided. The proposed model can be thus considered an adequate adaptation of Kecman's model for medium-thin-walled shapes.

This study also serves the purpose to continue the research into thin-walled structures used mainly in various industry, especially as it provides the means to predict the maximum load and energy absorption characteristics of SHS and RHS. In turn, this research can help with better design choices in early design stages; since the calculation times are in the order of seconds and offer better approximations than Kecman's model with nominal material data, whereas the time needed for the numerical simulations or experimental tests is in the order of hours. Better design choices early can result in lighter and safer structures.

Acknowledgments

D. Lavayen would like to recognize the financial support provided by CONCYTEC (Peru) and The World Bank, through the Pontifical Catholic University of Peru and FONDECYT (Peru):"Funding Contract N10-2018-FONDECYT/WB PhD programs in strategic and general areas". Part of this work was also funded

by the Comunidad de Madrid through the project 2020/00335/001.
The authors would also like to thank Dr. M. A. Martinez-Casanova from the Material Science Department at UC3M for his help during testing.

Appendix

Calculation of the maximum bending stress

The maximum bending stress is determined by first calculating the critical stress σ_{cr} as follows:

$$\sigma_{cr} = \frac{\pi^2 E}{12(1-\nu^2)} \left(5.23 + 0.16\frac{a}{b}\right) \left(\frac{a}{t}\right)^2 \tag{13}$$

The maximum bending moment is then determined, depending on the relationship between the critical stress with the effective yield strength. The equations below are taken from [3] and [8]. However, in the work of [8], it is stated that the condition of $\sigma_{cr} \geq 3\sigma_{Ye}$ is actually $\sigma_{cr} \geq 2\sigma_{Ye}$.

- If $\sigma_{cr} \leq \sigma_{Ye}$

$$M_m = \sigma_{Ye} t b^2 \left(\frac{2a + b + a^\star(3a/b + 2)}{3(a+b)}\right) \tag{14}$$

- else if $\sigma_{cr} \geq 3\sigma_{Ye}$

$$M_m = \sigma_{Ye} t \left(a(b-t) + 0.5(b-2t)^2\right) \tag{15}$$

- else $\sigma_{Ye} < \sigma_{cr} < 3\sigma_{Ye}$

$$M_p = \sigma_{Ye} t \left(a(b-t) + 0.5(b-2t)^2\right) \tag{16}$$

$$M_p' = \sigma_{Ye} t b(a + b/3) \tag{17}$$

$$M_m = M_p' + (M_p - M_p')\frac{\sigma_{cr} - \sigma_{Ye}}{2\sigma_{Ye}} \tag{18}$$

Energy terms corresponding to Kecman's collapse theory

The basic energy absorbed by hinge lines according to Kecman [4], and based on Fig. 1 is determined by multiplying the bending moment per unit length, the length of the hinge line, and the angle between the surfaces adjacent to the hinge line in question. Eight work terms are defined:

$$W_1 = W_{EF} + W_{GH} = 2m_p a \left[\pi/2 - \rho - \arcsin\left(1 - \frac{b}{h}\sin\rho\right)\right] \tag{19}$$

$$W_2 = W_{BC} = m_p a \left[\pi - 2\arcsin\left(1 - \frac{b}{h}\sin\rho\right)\right] \tag{20}$$

$$W_3 = W_{AB} + W_{CJ} = 2m_p \left(b\sin^2\rho - h\sin\rho + \sqrt{b\sin\rho\,(2h - b\sin\rho)}\cos\rho\right) \times \left(\pi - \rho - \arcsin\left(1 - \frac{b}{h}\sin\rho\right)\right) \tag{21}$$

$$W_4 = W_{BG} + W_{BE} + W_{CH} + W_{CF} = 4m_p h\pi/2 \tag{22}$$

$$W_5 = W_{GK} + W_{EL} + W_{HN} + W_{FM} = 4m_p b \arctan\left[\frac{z_A}{\sqrt{(h - x_A")^2 + (y_A" - y_B)^2}}\right] \tag{23}$$

$$W_6 = W_{GA} + W_{AE} + W_{CH} + W_{CF} = 4m_p \frac{h}{r} z_A \tag{24}$$

$$W_7 = W_{KA} + W_{LA} + W_{NJ} + W_{MJ} = \frac{8}{3} m_p \frac{z_A}{r}\sqrt{h^2 + y_b^2 + z_A^2} \tag{25}$$

$$W_8 = W_{KN} + W_{LM} + W_{KL} + W_{MN} = 2m_p \left(a\rho + 2h\arctan\left(\frac{z_A}{y_A}\right)\right) \tag{26}$$

References

[1] B. Klein, Leichtbau-Konstruktion: Berechnungsgrundlagen und Gestaltung, 10th Edition, Springer, Wiesbaden, 2013.

[2] H. E. Friedrich, Leichtbau in der Fahrzeugtechnik, 2nd Edition, Springer, Wiesbaden, 2017. doi:10.1007/978-3-658-12295-9.

[3] D. Kecman, Bending collapse of rectangular section tubes in relation to the bus roll over problem, Phd thesis, Cranfield Insititute of Technology (1979).

[4] D. Kecman, Bending collapse of rectangular and square section tubes, International Journal of Mechanical Sciences 25 (9-10) (1983) 623–636. doi:10.1016/0020-7403(83)90072-3.

[5] T. Wierzbicki, W. Abramowicz, On the Crushing Mechanics of Thin-Walled Structures, Journal of Applied Mechanics 50 (4a) (1983) 727–734. doi:10.1115/1.3167137.

[6] T. Wierzbicki, L. Recke, W. Abramowicz, T. Gholami, J. Huang, Stress profiles in thin-walled prismatic columns subjected to crush loading-I. Compression, Computers and Structures 51 (6) (1994) 625–641. doi:10.1016/S0045-7949(05)80002-1.

[7] T. Wierzbicki, L. Recke, W. Abramowicz, T. Gholami, J. Huang, Stress profiles in thin-walled prismatic columns subjected to crush loading-II. Bending, Computers and Structures 51 (6) (1994) 625–641. doi:10.1016/S0045-7949(05)80002-1.

[8] T. H. Kim, S. R. Reid, Bending collapse of thin-walled rectangular section columns, Computers and Structures 79 (20-21) (2001) 1897–1911. doi:10.1016/S0045-7949(01)00089-X.

[9] K. C. Shin, J. J. Lee, K. H. Kim, M. C. Song, J. S. Huh, Axial crush and bending collapse of an aluminum/GFRP hybrid square tube and its

energy absorption capability, Composite Structures 57 (1-4) (2002) 279–287. doi:10.1016/S0263-8223(02)00094-6.

[10] Y. Liu, M. L. Day, Bending collapse of thin-walled circular tubes and computational application, Thin-Walled Structures 46 (4) (2008) 442–450. doi:10.1016/j.tws.2007.07.014.

[11] H. C. Kim, D. K. Shin, J. J. Lee, Characteristics of aluminum/CFRP short square hollow section beam under transverse quasi-static loading, Composites Part B: Engineering 51 (2013) 345–358. doi:10.1016/j.compositesb.2013.03.020.

[12] Z. Huang, X. Zhang, Three-point bending collapse of thin-walled rectangular beams, International Journal of Mechanical Sciences 144 (April) (2018) 461–479. doi:10.1016/j.ijmecsci.2018.06.001.

[13] Z. Huang, X. Zhang, X. Fu, On the bending force response of thin-walled beams under transverse loading, Thin-Walled Structures 154 (March) (2020) 106807. doi:10.1016/j.tws.2020.106807.

[14] J. C. Brown, G. H. Tidbury, An investigation of the collapse of thin walled rectangular beams in biaxial bending, International Journal of Mechanical Sciences 25 (9) (1983) 733–746.

[15] S. H. Lee, H. J. Kim, N. S. Choi, Bending performance analysis of aluminum-composite hybrid tube beams, Key Engineering Materials 306-308 II (2006) 769–774. doi:10.4028/www.scientific.net/KEM.306-308.769.

[16] S. H. Lee, C. W. Kim, N. S. Choi, Bending collapse behaviors and energy absorption characteristics of aluminum-GFRP hybrid tube beams, Key Engineering Materials 326-328 II (2006) 1825–1828. doi:10.4028/www.scientific.net/kem.326-328.1825.

[17] S. Ruiz, P. Cruz, B. Sorita, H. Vida, New Optimized Bus Structure to Improve the Roll-Over Test (ECE-R66) Using Structural Foam with High

Strength Steel, SAE Technical Papers 2009-Janua (January) (2009). doi:10.4271/2009-26-0003.

[18] S. Eksi, K. Genel, Bending response of hybrid composite tubular beams, Thin-Walled Structures 73 (2013) 329–336. doi:10.1016/j.tws.2013.09.001.

[19] A. M. Kadir, D. Priadi, E. S. Siradj, H. Setiyono, Developing a strength analytical method of a thin-walled steel SHS beam by combine theory of plastic mechanisms and non-linear elastic, Advanced Materials Research 746 (2013) 428–433. doi:10.4028/www.scientific.net/AMR.746.428.

[20] V. D. Phadatare, P. Hujare, Performance Improvement of Bus Structure for Rollover Analysis Using FEA and Validation of Roll Bar, IOSR Journal of Mechanical and Civil Engineering 17 (10) (2017) 16–19. doi:10.9790/1684-17010041619.

[21] Q. Liu, X. Xu, J. Ma, J. Wang, Y. Shi, D. Hui, Lateral crushing and bending responses of CFRP square tube filled with aluminum honeycomb, Composites Part B: Engineering 118 (2017) 104–115. doi:10.1016/j.compositesb.2017.03.021.

[22] Z. Huang, X. Zhang, Crashworthiness and optimization design of quadruple-cell Aluminum/CFRP hybrid tubes under transverse bending, Composite Structures 235 (2020) 111753. doi:10.1016/j.compstruct.2019.111753.

[23] Z. Huang, X. Zhang, C. Yang, Experimental and numerical studies on the bending collapse of multi-cell Aluminum/CFRP hybrid tubes, Composites Part B: Engineering 181 (2020) 107527. doi:10.1016/j.compositesb.2019.107527.

[24] Z. you Xie, The reinforcement optimization of thin-walled square tubes for bending crashworthiness, International Journal of Crashworthiness 0 (0) (2020) 1–7. doi:10.1080/13588265.2020.1766186.

[25] UN/ECE 66, Regulation No 66 of the Economic Commission for Europe of the United Nations (EN/ECE) - Uniform technical prescriptions concerning the approval of large passenger vehicles with regard to the strength of their superstructure (2007).

[26] S. M. Hashemi, A. C. Waltona, K. Kayvantash, Strength of super-structure UN-ECE R66 rollover approval of coaches based on thin-walled framework structures, International Journal of Vehicle Structures and Systems 1 (4) (2009) 78–84. doi:10.4273/ijvss.1.4.04.

[27] C. C. Liang, G. N. Le, Bus rollover crashworthiness under European standard: An optimal analysis of superstructure strength using successive response surface method, International Journal of Crashworthiness 14 (6) (2009) 623–639. doi:10.1080/13588260902920670.

[28] C. C. Liang, G. N. Le, Optimization of bus rollover strength by consideration of the energy absorption ability, International Journal of Automotive Technology 11 (2) (2010) 173–185. doi:10.1007/s12239-010-0023-3.

[29] C. C. Liang, G. N. Le, Analysis of bus rollover protection under legislated standards using LS-DYNA software simulation techniques, International Journal of Automotive Technology 11 (4) (2010) 495–506. doi:10.1007/s12239-010-0061-x.

[30] D. Rincón-Dávila, E. Alcalá, Á. Martín, Theoretical-experimental study of the repair of steel bus structures after rollover, Journal of Constructional Steel Research 162 (2019) 105734. doi:10.1016/j.jcsr.2019.105734.

[31] ANSYS Inc., ANSYS as a Server Example: MATLAB Setup (2019).

[32] X. Zhang, H. Zhang, W. Ren, Bending collapse of folded tubes, International Journal of Mechanical Sciences 117 (2016) 67–78. doi:10.1016/j.ijmecsci.2016.07.016.

[33] P. Krolo, D. Grandić, Ž. Smolčić, Experimental and Numerical Study of Mild Steel Behaviour under Cyclic Loading with Variable Strain Ranges,

Advances in Materials Science and Engineering 2016 (2016). doi:10.1155/2016/7863010.

[34] W. Abramowicz, N. Jones, Transition from initial global bending to progressive buckling of tubes loaded statically and dynamically, International Journal of Impact Engineering 19 (5-6) (1997) 415–437. doi:10.1016/s0734-743x(96)00052-8.